Supplementary Information for
Probing spin hydrodynamics on a superconducting quantum simulator

Yun-Hao Shi,[1,2,3,*] Zheng-Hang Sun,[1,2,*] Yong-Yi Wang,[1,2,*] Zheng-An Wang,[3,4] Yu-Ran Zhang,[5] Wei-Guo Ma,[1,2] Hao-Tian Liu,[1,2] Kui Zhao,[3] Jia-Cheng Song,[1,2] Gui-Han Liang,[1,2] Zheng-Yang Mei,[1,2] Jia-Chi Zhang,[1,2] Hao Li,[3] Chi-Tong Chen,[1,2] Xiaohui Song,[1] Jieci Wang,[6] Guangming Xue,[3] Haifeng Yu,[3] Kaixuan Huang,[3,†] Zhongcheng Xiang,[1,2,4,‡] Kai Xu,[1,2,3,4,7,8,§] Dongning Zheng,[1,2,4,7,8] and Heng Fan[1,2,3,4,7,8,¶]

[1] *Institute of Physics, Chinese Academy of Sciences, Beijing 100190, China*
[2] *School of Physical Sciences, University of Chinese Academy of Sciences, Beijing 100049, China*
[3] *Beijing Academy of Quantum Information Sciences, Beijing 100193, China*
[4] *Hefei National Laboratory, Hefei 230088, China*
[5] *School of Physics and Optoelectronics, South China University of Technology, Guangzhou 510640, China*
[6] *Department of Physics and Key Laboratory of Low Dimensional Quantum Structures and Quantum Control of Ministry of Education, Hunan Normal University, Changsha, Hunan 410081, China*
[7] *Songshan Lake Materials Laboratory, Dongguan, Guangdong 523808, China*
[8] *CAS Center for Excellence in Topological Quantum Computation, UCAS, Beijing 100190, China*

CONTENTS

* These authors contributed equally to this work.
† huangkx@baqis.ac.cn
‡ zcxiang@iphy.ac.cn
§ kaixu@iphy.ac.cn
¶ hfan@iphy.ac.cn

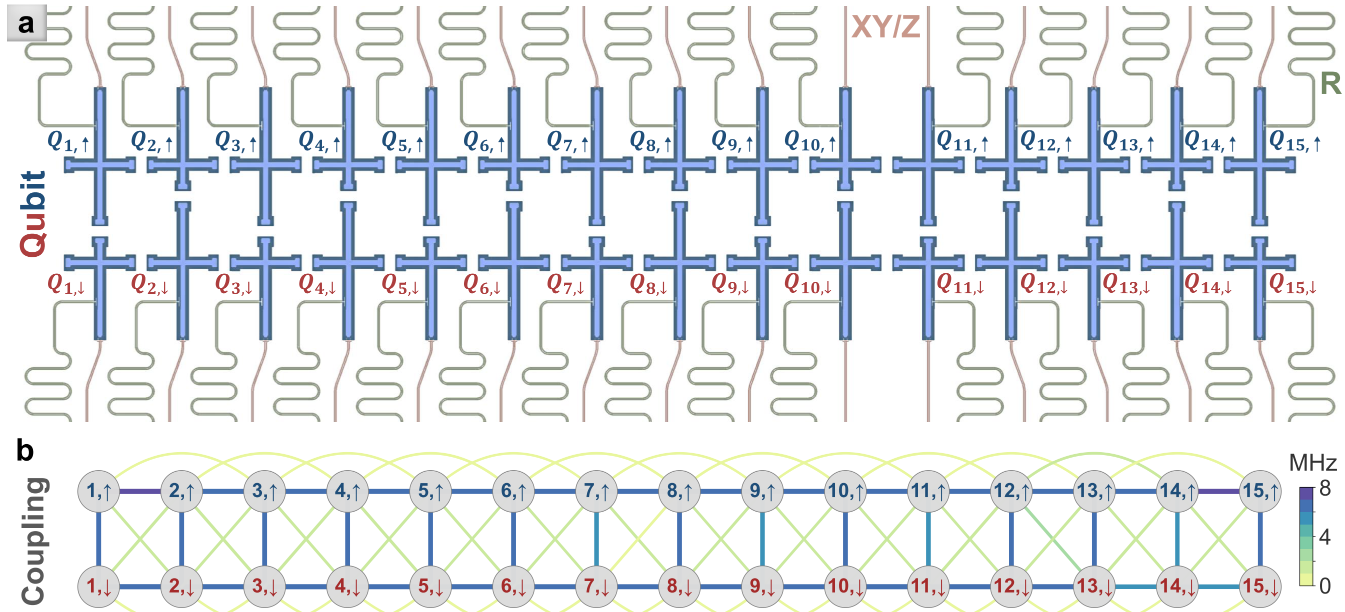

FIG. S1. **Schematic and coupling strengths of the chip. a**, The ladder-type chip with 30 superconducting qubits arranged in two coupled chains. Each qubit, coupled to an independent readout resonator R, has an independent microwave line for XY and Z controls. **b**, Coupling strengths including the NN and NNN hopping couplings, which are measured by swapping experiments at the resonant frequency $\omega_{\text{ref}} \approx 4.534\,\text{GHz}$.

Supplementary Note 1. MODEL AND HAMILTONIAN

In this experiment, we use a ladder-type superconducting quantum processor with 30 programmable superconducting transmon qubits, which is identical to the device in ref. [22]. The optical micrograph and coupling strengths of the chip are shown in Fig. S1, and the device parameters are listed in Table S1. The Hamiltonian of the total system can be essentially described by a Bose-Hubbard model of a ladder

$$\hat{H}_{\text{BH}} = \sum_{i=1}^{N} \hbar h_i \hat{a}_j^\dagger \hat{a}_j - \frac{E_{\text{C},j}}{2} \hat{a}_j^\dagger \hat{a}_j^\dagger \hat{a}_j \hat{a}_j + \hat{H}_I, \tag{S1}$$

where $\hbar$ is the reduced Planck constant, N is the total number of qubits, $\hat{a}^\dagger$ $(\hat{a})$ denotes the bosonic creation (annihilation) operator, h_j is the tunable on-site potential, $E_{\text{C},j}$ denotes the on-site charge energy, representing the magnitude of anharmonicity, and $\hat{H}_I$ is the Hamiltonian for the interactions between qubits. For qubits connected in a ladder-type with two coupled chains ('$\uparrow$' and '$\downarrow$'), the interaction Hamiltonian $\hat{H}_I$ is mainly derived from the nearest-neighbor (NN) rung (vertical, '$\perp$') and intrachain (parallel, '$\|$') hopping couplings, namely

$$\hat{H}_\perp = \sum_{j=1}^{L} \hbar J_j^\perp (\hat{a}_{j,\uparrow}^\dagger \hat{a}_{j,\downarrow} + \text{H.c.}), \tag{S2}$$

$$\hat{H}_\| = \sum_{m\in\{\uparrow,\downarrow\}} \sum_{j=1}^{L-1} \hbar J_{j,m}^\| (\hat{a}_{j,m}^\dagger \hat{a}_{j+1,m} + \text{H.c.}), \tag{S3}$$

where $L = N/2$ is the length of each chain, $J_j^\perp$ and $J_{j,m}^\|$ are the NN rung and intrachain coupling strengths. The mean values of $J_j^\perp/2\pi$ and $J_{j,m}^\|/2\pi$ are 6.6 MHz and 7.3 MHz, respectively. In addition, it is inevitable that small next-nearest-neighbor (NNN) interactions are present, including the hopping interactions between the diagonal qubits of the upper and lower chains ('$\times$', diagonal down '$\diagdown$' and diagonal up '$\diagup$') and between NNN qubits on each chain ('$\cap$'), and the corresponding Hamiltonians are expressed as

$$\hat{H}_{\times} = \sum_{j=1}^{L-1} \hbar J_j^{\searrow} (\hat{a}_{j,\uparrow}^{\dagger}\hat{a}_{j+1,\downarrow} + \text{H.c.}) + \hbar J_j^{\nearrow} (\hat{a}_{j,\downarrow}^{\dagger}\hat{a}_{j+1,\uparrow} + \text{H.c.}), \tag{S4}$$

$$\hat{H}_{\cap} = \sum_{m\in\{\uparrow,\downarrow\}} \sum_{j=1}^{L-2} \hbar J_{j,m}^{\cap} (\hat{a}_{j,m}^{\dagger}\hat{a}_{j+2,m} + \text{H.c.}), \tag{S5}$$

where $J_j^{\searrow}$, $J_j^{\nearrow}$ and $J_{j,m}^{\cap}$ are the strengths of diagonal down, diagonal up and parallel NNN hopping interactions, respectively. In short, for numerical simulations, we consider $\hat{H}_I = \hat{H}_{\perp} + \hat{H}_{\parallel} + \hat{H}_{\times} + \hat{H}_{\cap}$.

In our quantum processor, the anharmonicity ($\geq 200\,\text{MHz}$) is much greater than the coupling interaction and the model can be viewed as a ladder-type lattice of hard-core bosons [52], i.e., the Eq. (1) in the main text. However, in principle, the leakage to higher occupation states can be possibly induced by the finite value of the ratio between the averaged anharmonicity and coupling strength, i.e., $\overline{E_C}/\overline{J}$. To qualitatively characterize whether the Bose-Hubbard model (S1) can be approximate as the hard-core bosons, we consider the dynamics of the summation of the probability $\sum_{\max(\vec{s})=1} p(\vec{s})$ with $\vec{s}$ denoting a configuration of product state. For instance, $\vec{s} = (1,0,1,0,...,1,0)$ corresponds to the Néel state $|\vec{s}\rangle = |1010...10\rangle$. If the system exactly becomes a hard-core bosonic model, $\sum_{\max(\vec{s})=1} p(\vec{s}) = 1$. Here, we numerically simulate the dynamics of $\sum_{\max(\vec{s})=1} p(\vec{s})$ for the Hamiltonian of the superconducting circuit with experimentally measured hopping interactions and anharmonicity. As an example, we adopt the system size $L = 16$ and a half-filling product state as the initial state $|\psi_0\rangle$ (see the inset of Fig. S2**a**). The results are plotted in Fig. S2**a**. One can see that the summation of the probabilities for the states with higher occupations, i.e., $\sum_{\max(\vec{s})>1} p(\vec{s}) = 1 - \sum_{\max(\vec{s})=1} p(\vec{s})$, only reach a relatively small value ~ 0.03, with the evolved time $t \simeq 200$ ns. Moreover, we numerically simulate the time evolution of the particle number $\langle n(t)\rangle \equiv \langle\psi(t)|\hat{n}|\psi(t)\rangle = \langle\psi(t)|\sum_i \hat{n}_i|\psi(t)\rangle$, with $\hat{n}_i \equiv |0\rangle_i\langle 0| + |1\rangle_i\langle 1|$, up to the experimental time scales $t \simeq 200$ ns. The results are displayed in Fig. S2**b**. We emphasize that only the occupations of the states $|0\rangle$ and $|1\rangle$ are considered in the definition of $\hat{n}_i$, while the finite $\overline{E_C}/\overline{J}$ allows the possibility of the leakage to the states with higher occupations, such as $|2\rangle$. Consequently, the decay of $\langle n(t)\rangle$ shown in Fig. S2 quantifies the leakage induced by the finite $\overline{E_C}/\overline{J}$. The stable value of $n(t)/2L$ with $t \simeq 200$ ns is about 0.4966, indicating a moderate impact of the leakage on the conservation of the particle number. In short, the results in Fig. S2 suggest that hard-core bosonic Hamiltonian (1) in the main text, with a conservation of the particle number, can efficiently describe our superconducting quantum simulator.

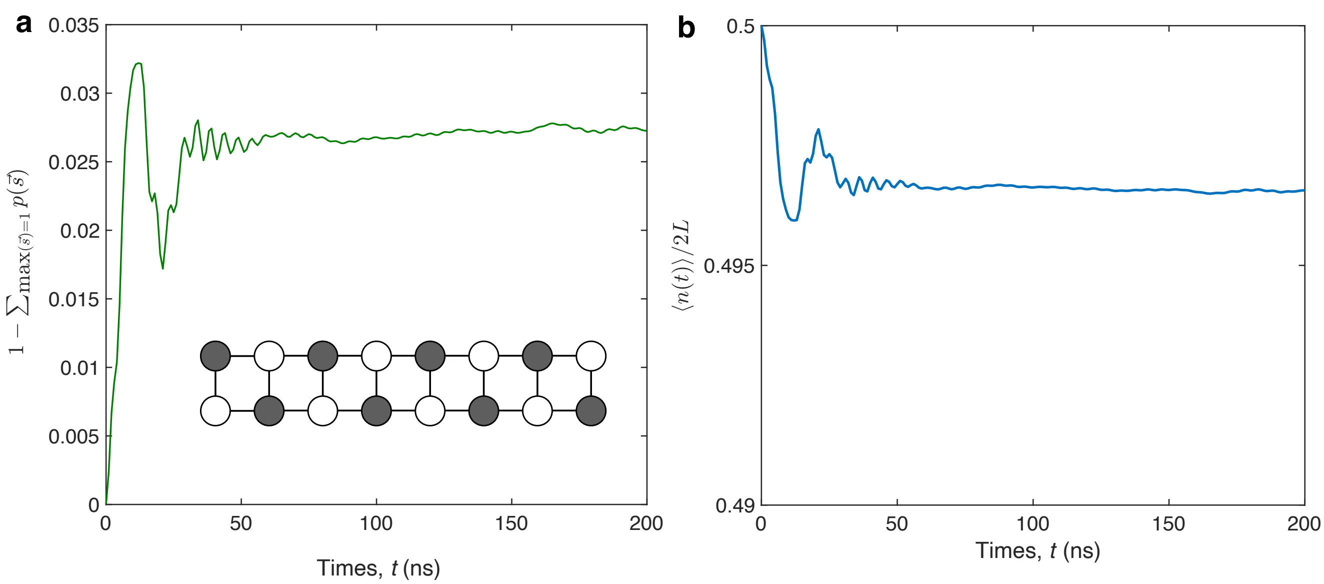

FIG. S2. **Demonstrate of hard-core bosonic model. a**, Time evolution of $\sum_{\max(\vec{s})=1} p(\vec{s})$ for the Hamiltonian of the superconducting circuit described by the Bose-Hubbard model (S1), with a system size $L = 8$. The inset shows a schematic of the chosen initial state, where the sites represented with solid black circuits are initialized by the state $|1\rangle$, and the remainder sites are initialized by $|0\rangle$. **b**, The dynamics of the particle number $\langle n(t)\rangle$ for the Hamiltonian of the superconducting circuit with a system size $L = 8$.

Parameter	Median	Mean	Stdev.	Units
Qubit maximum frequency	5.025	5.032	0.240	GHz
Qubit idle frequency	4.723	4.728	0.346	GHz
Qubit anharmonicity $-E_{\mathrm{C}}/(2\pi\hbar)$	-0.222	-0.222	0.022	GHz
Readout frequency	6.715	6.714	0.061	GHz
Mean energy relaxation time $\overline{T}_1$	33.2	32.1	7.5	μs
Pure dephasing time at idle frequency T_2^*	1.0	2.4	4.2	μs
Mean NN hopping coupling strength (vertical) $\overline{J^{\perp}}$	6.7	6.6	0.2	MHz
Mean NN hopping coupling strength (parallel) $\overline{J^{\parallel}}$	7.2	7.3	0.1	MHz
Mean NNN hopping coupling strength (diagonal) $\overline{J^{\times}}$	1.5	1.5	0.3	MHz
Mean NNN hopping coupling strength (parallel) $\overline{J^{\cap}}$	0.6	0.7	0.2	MHz
Readout fidelity of state $\|0\rangle$	95.2	91.4	9.6	%
Readout fidelity of state $\|1\rangle$	88.5	84.7	9.3	%

TABLE S1. **List of device parameters.**

Supplementary Note 2. WIRING INFORMATION

The typical wiring information is shown in Fig. S3, in which from up to down are the control lines of qubit (XY and Z), readout, and Josephson parametric amplifier (JPA), respectively. From left to right, the ambient temperature decreases from room temperature to $12\,\mathrm{mK}$ in a BlueFors XLD-1000 dilution refrigerator. We combine the high-frequency XY signal with the low-frequency Z bias by using directional couplers at room temperature. The XY signals are generated via frequency mixing. In detail, we use the IQ mixer to mix the intrinsic local oscillation (LO) from a microwave signal source and the IQ signals generated from two channels of arbitrary waveform generator (AWG). The output microwave signal is programmable, which depends on the pulses written into IQ signals. The joint readout signals are sent through the transmission line and amplified by the JPA, a cryo low-noise amplifier (LNA) and a room-temperature RF amplifier (RFA), and finally demodulated by the analog-digital converter (ADC).

Supplementary Note 3. XY DRIVE IN SUPERCONDUCTING CIRCUITS

A. Single-qubit XY drive

A transmon qubit is composed of a capacitance C and a nonlinear inductance L (Josephson junction or SQUID). Its Lagrangian $\mathcal{L}_0$ and Hamiltonian H_0 can be written as

$$\mathcal{L}_0 = \frac{Q^2}{2C} - \frac{\Phi^2}{2L} \tag{S6}$$

$$H_0 = \frac{Q^2}{2C} + \frac{\Phi^2}{2L}, \tag{S7}$$

where $Q = \partial\mathcal{L}_0/\partial\dot{\Phi} = C\dot{\Phi}$ denotes the charge, and Φ is the magnetic flux of the circuit. Here, the nonlinear inductance of the Josepshon junction with energy E_{J} can be written as $L = L_{\mathrm{c}}/\cos(2\pi\Phi/\Phi_0)$, where $\Phi_0 = \hbar\pi/\mathrm{e}$ is the superconducting flux quantum, $\mathrm{e} \approx 1.602\times10^{-19}\mathrm{C}$ is the electron charge, and $L_{\mathrm{c}} = \Phi_0^2/(4\pi^2 E_{\mathrm{J}})$ is the constant inductance. This nonlinear inductance can be easily derived from the definition $L = \mathrm{d}\Phi/\mathrm{d}I$ and the Josephson equation $I = I_{\mathrm{c}}\sin(2\pi\Phi/\Phi_0)$ with $I_{\mathrm{c}} = 2\pi E_{\mathrm{J}}/\Phi_0$ being the Josephson critical current.

Considering the weak flux Φ, one can use the approximation $\cos(2\pi\Phi/\Phi_0) \simeq 1 - (2\pi\Phi/\Phi_0)^2/2$ and reduce the Hamiltonian Eq. (S7) into $H_0 \simeq \frac{Q^2}{2C} + \frac{\Phi^2}{2L_{\mathrm{c}}} - \frac{\pi^2\Phi^4}{4L_{\mathrm{c}}\Phi_0^2}$, which can be viewed as a harmonic oscillator with $o(\Phi^4)$ perturbation. Using canonical quantization, one can introduce

$$\begin{cases} \hat{Q} = \mathrm{i}Q_{\mathrm{zpf}}(\hat{a}^\dagger - \hat{a}) \\ \hat{\Phi} = \Phi_{\mathrm{zpf}}(\hat{a}^\dagger + \hat{a}) \end{cases} \tag{S8}$$

with $Q_{\mathrm{zpf}} = \sqrt{\hbar(C/L_{\mathrm{c}})^{\frac{1}{2}}/2}$ and $\Phi_{\mathrm{zpf}} = \sqrt{\hbar(L_{\mathrm{c}}/C)^{\frac{1}{2}}/2}$ being the zero point fluctuation of the charge and flux operators,

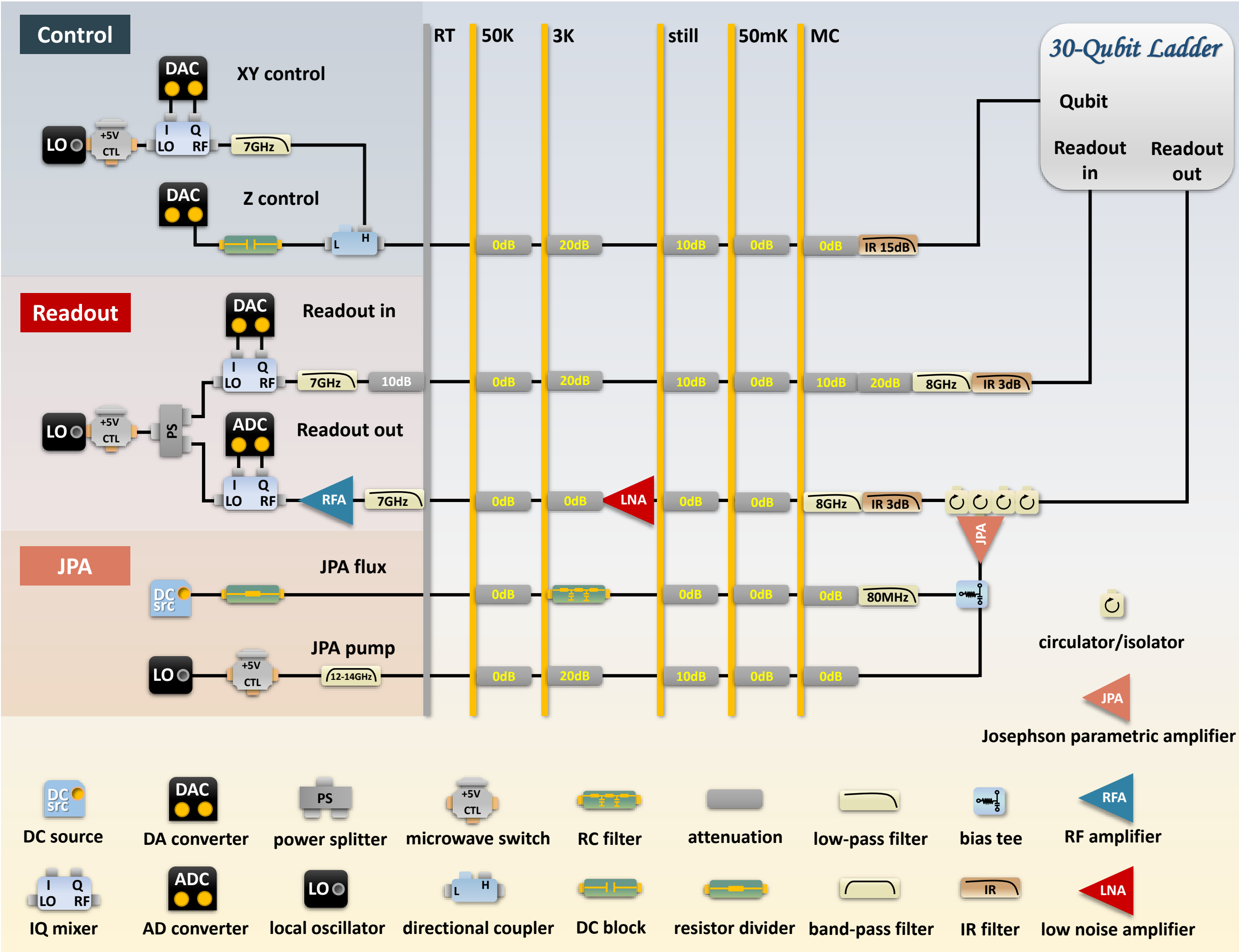

FIG. S3. **Schematic diagram of the experimental system and wiring information.**

respectively. The quantized Hamiltonian thus is (the constant term is omitted):

$$\hat{H}_0 = \hbar\omega\hat{a}^\dagger\hat{a} - \frac{E_\mathrm{C}}{2}\hat{a}^\dagger\hat{a}^\dagger\hat{a}\hat{a}, \tag{S9}$$

where $\omega = (\sqrt{8E_\mathrm{C}E_\mathrm{J}} - E_\mathrm{C})/\hbar$ denotes the qubit frequency, and $E_\mathrm{C} = \mathrm{e}^2/(2C)$ is the charging energy that represents the magnitude of anharmonicity. For a single Josephson junction, E_J is not tunable, while for a SQUID with two junctions, it depends on the external flux Φ_ext applied to the junction region. In the experiments, we can adjust the qubit frequency ω via the external fast flux bias applied to the Z control line.

When a time-dependent driving voltage $V_\mathrm{d}(t)$ is added into a transmon qubit (Fig. S4), the driving current I_d can be split into the qubit capacitance term I_C and the Josephson junction term I_J. Meanwhile, according to Kirchhoff voltage law, the total voltage reduction through either of the two branches must be zero. Thus, one can obtain the following motion equation

$$\begin{cases} I_\mathrm{d} = I_\mathrm{C} + I_\mathrm{J} \\ -\dot{V}_\mathrm{d} + \frac{I_\mathrm{d}}{C_\mathrm{d}} + \frac{I_\mathrm{C}}{C} = 0 \\ -\dot{V}_\mathrm{d} + \frac{I_\mathrm{d}}{C_\mathrm{d}} + L\dot{I}_\mathrm{J} = 0 \end{cases} \Rightarrow \ \ddot{\Phi} + \frac{1}{C_\Sigma L}\Phi - \frac{C_\mathrm{d}\dot{V}_\mathrm{d}(t)}{C_\Sigma} = 0, \tag{S10}$$

where $C_\Sigma = C + C_\mathrm{d}$, $\Phi = LI_\mathrm{J}$. Here C, C_d and L are the qubit capacitance, the driving capacitance, and the nonlinear inductance, respectively. The above equation can be viewed as the Euler-Lagrange equation: $\frac{\partial\mathcal{L}_\mathrm{driven}}{\partial\Phi} - \frac{\mathrm{d}}{\mathrm{d}t}\frac{\partial\mathcal{L}_\mathrm{driven}}{\partial\dot{\Phi}} = 0$, where the Lagrangian of this driven qubit can be constructed as

$$\mathcal{L}_\mathrm{driven} = \frac{1}{2}C\dot{\Phi}^2 + \frac{1}{2}C_\mathrm{d}\left(V_\mathrm{d}(t) - \dot{\Phi}\right)^2 - \frac{\Phi^2}{2L}, \tag{S11}$$

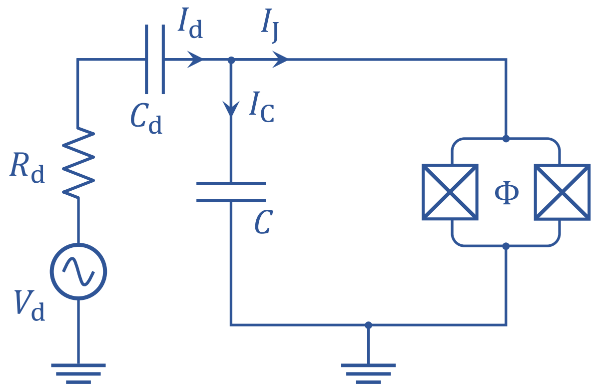

FIG. S4. **Circuit diagram of a driven transmon qubit.** The qubit is coupled to a time-dependent driving voltage $V_{\rm d}$. The capacitances of the qubit and the drive are labeled as C and $C_{\rm d}$, respectively. The magnetic flux threading the loop is denoted as Φ. The driving current $I_{\rm d}$ is split into $I_{\rm C}$ and $I_{\rm J}$.

where $C_{\rm d}$ is the driving capacitance. In Eq. (S11), the first term represents the charge energy of C, the second term denotes the charge energy of $C_{\rm d}$ caused by induced electromotive force, and the last term is the inductance energy of L.

To obtain the Hamiltonian, we first calculate the conjugate to the position (flux) Φ, namely the canonical momentum (charge) $\tilde{Q} = \partial\mathcal{L}_{\rm driven}/\partial\dot{\Phi} = C_\Sigma\dot{\Phi} - C_{\rm d}V_{\rm d}(t)$, and thus

$$H_{\rm driven} = \tilde{Q}\dot{\Phi} - \mathcal{L}_{\rm driven} = \frac{\tilde{Q}}{2C_\Sigma} + \frac{\Phi^2}{2L} + \frac{\tilde{Q}C_{\rm d}V_{\rm d}(t)}{C_\Sigma}. \tag{S12}$$

Using the canonical quantization procedure like Eq. (S8), we introduce $\hat{\tilde{Q}} = {\rm i}\tilde{Q}_{\rm zpf}(\hat{a}^\dagger - \hat{a})$ and $\hat{\Phi} = \Phi_{\rm zpf}(\hat{a}^\dagger + \hat{a})$ to quantize the driven system, where $\tilde{Q}_{\rm zpf} = \sqrt{\hbar(C_\Sigma/L_{\rm c})^{\frac{1}{2}}/2}$ and $\Phi_{\rm zpf} = \sqrt{\hbar(L_{\rm c}/C_\Sigma)^{\frac{1}{2}}/2}$. Hence, the Hamiltonian becomes

$$\hat{H}_{\rm driven} = \hbar\omega\hat{a}^\dagger\hat{a} - \frac{E_{\rm C}}{2}\hat{a}^\dagger\hat{a}^\dagger\hat{a}\hat{a} + {\rm i}\hbar\Omega(t)(\hat{a}^\dagger - \hat{a}), \tag{S13}$$

where $E_{\rm C} = {\rm e}^2/(2C_\Sigma)$, $E_{\rm J} = \Phi_0^2/(4\pi^2 L_{\rm c})$, $\omega = (\sqrt{8E_{\rm C}E_{\rm J}} - E_{\rm C})/\hbar$, $\Omega(t) = \epsilon V_{\rm d}(t)$, $\epsilon = \tilde{Q}_{\rm zpf}C_{\rm d}/(\hbar C_\Sigma)$. Here, we set the time-dependent driving $V_{\rm d}(t) = -V_{\rm d}\sin(\omega_{\rm d}t + \phi) = {\rm Im}\{V_{\rm d}e^{-{\rm i}(\omega_{\rm d}t+\phi)}\}$, thus $\Omega(t) = {\rm i}\Omega\left(e^{{\rm i}(\omega_{\rm d}t+\phi)} - e^{-{\rm i}(\omega_{\rm d}t+\phi)}\right)/2$, where $\Omega = \epsilon V_{\rm d}$ is so-called Rabi frequency. The parameter ϵ represents the Rabi frequency corresponding to the unit amplitude of the drive.

To solve the time evolution governed by the above time-dependent Hamiltonian, we consider the rotating frame which is generated by $\hat{U}_d(t) = e^{{\rm i}\omega_{\rm d}t\hat{a}^\dagger\hat{a}}$

$$\begin{aligned}\hat{H}_d &= \hat{U}_d(t)\hat{H}_{\rm driven}(t)\hat{U}_d^\dagger(t) + {\rm i}\hbar\left(\frac{\rm d}{{\rm d}t}\hat{U}_d(t)\right)\hat{U}_d^\dagger(t)\\ &\simeq \hbar\Delta\hat{a}^\dagger\hat{a} - \frac{E_{\rm C}}{2}\hat{a}^\dagger\hat{a}^\dagger\hat{a}\hat{a} + \frac{\hbar\Omega}{2}\left(\hat{a}^\dagger e^{-{\rm i}\phi} + \hat{a}e^{{\rm i}\phi}\right),\end{aligned} \tag{S14}$$

where $\Delta = \omega - \omega_{\rm d}$ is the frequency detuning, and the rotating-wave approximation is adopted by ignoring high frequency oscillation $\pm 2\omega_{\rm d}$.

With $\Delta = 0$ and $E_{\rm C} \gg \Omega$, the large anharmonicity results in the resonant drive acting almost exclusively between the first two energy levels $|0\rangle$ and $|1\rangle$ without leakage to higher levels. Hence, considering the two-level qubit, we have

$$\hat{H}_d = \frac{\hbar\Omega}{2}\left(\hat{\sigma}^+ e^{-{\rm i}\phi} + \hat{\sigma}^- e^{{\rm i}\phi}\right), \tag{S15}$$

where $\hat{\sigma}_j^+$ $(\hat{\sigma}_j^-)$ is the raising (lowering) operator. If the qubit begins in the ground state $|0\rangle$, its time-dependent state during the unitary evolution is

$$|\psi_d(t)\rangle = e^{-\frac{\rm i}{\hbar}\hat{H}_d t}|0\rangle = \cos\frac{\Omega t}{2}|0\rangle - {\rm i}e^{{\rm i}\phi}\sin\frac{\Omega t}{2}|1\rangle, \tag{S16}$$

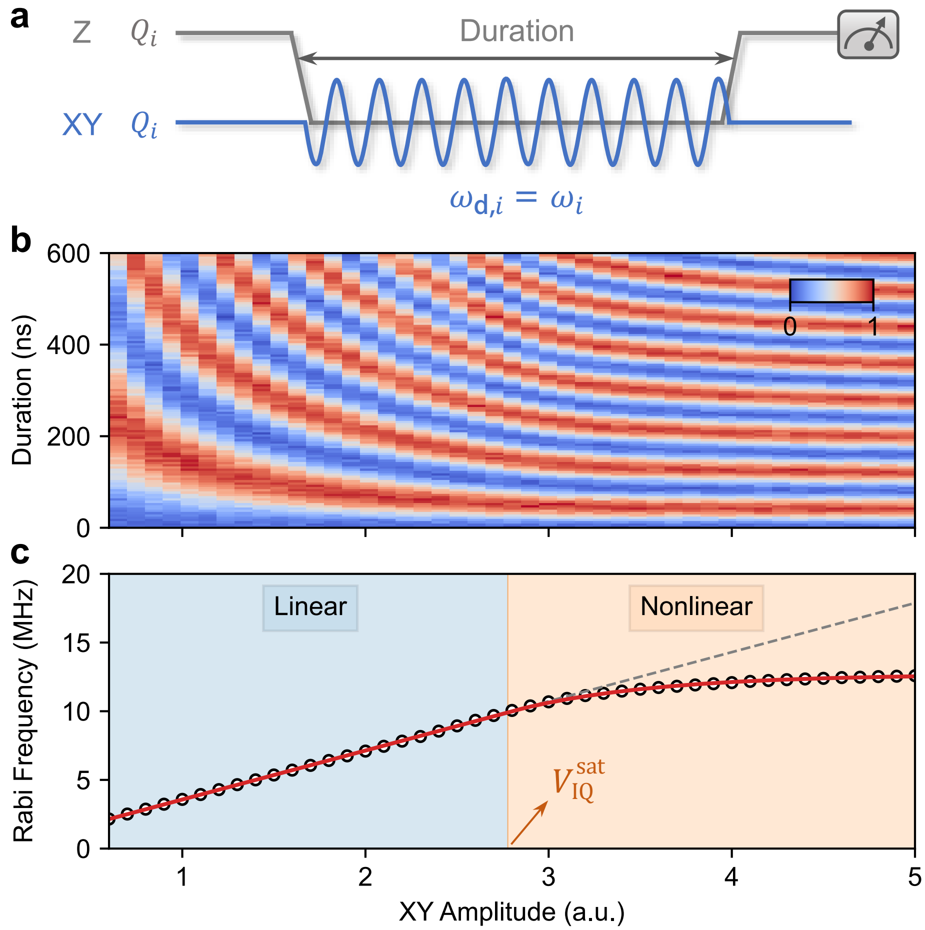

FIG. S5. **Typical experimental data of measuring the relationship between Rabi frequency and XY drive amplitude. a**, Experimental pulse sequence. Qubit is detuned from its idle frequency to the operating ω_i. Meanwhile, we apply resonant microwave drives on this qubit with scanning XY amplitude V_{IQ} and measure the vacuum Rabi oscillations shown in **b**. **b**, The heatmap of the probabilities of qubit in the state $|1\rangle$ as a function of duration and XY amplitude. **c**, For each XY drive amplitude, we fit the curve of vacuum Rabi oscillation by using Eq. (S17) to obtain the experimental Rabi frequency, denoted as black hollow circle. The red solid line is the result of fitting the experimental Rabi frequencies by using a smooth piecewise function and the grey dashed line implies the linear relationship between Rabi frequency and XY drive amplitude when the drive amplitude is less than $V_{\mathrm{IQ}}^{\mathrm{sat}}$.

and the probability of qubit in $|1\rangle$ is given by $P_1(t) = \sin^2(\Omega t/2) = [1 - \cos(\Omega t)]/2$. Considering the energy relaxation, the envelope of $P_1(t)$ will decay in a dissipative evolution and thus

$$P_1(t) = \frac{1}{2}\left[1 - e^{-\frac{t}{T_1}}\cos(\Omega t)\right], \tag{S17}$$

where T_1 is the energy relaxation time that depends on the qubit frequency ω. In order to obtain the Rabi frequency Ω, one can fit the data of $P_1(t)$ by using the form of function $A\exp(-t/T_1)\cos(\Omega t) + B$. Typical experimental data of calibrating XY drive with different driving amplitudes are displayed in Fig. S5.

The above results are based on the resonance condition $\omega = \omega_{\mathrm{d}}$. If the detuning $\Delta = \omega - \omega_{\mathrm{d}} \neq 0$, the effective Rabi frequency will be

$$\Omega_{\mathrm{R}} = \sqrt{\Delta^2 + \Omega^2}. \tag{S18}$$

Therefore, to obtain the correct Rabi frequency when $\omega = \omega_{\mathrm{d}}$, we should find the corresponding Z pulse amplitude that makes the qubit resonate with the microwave before calibrating XY drive. This step can be easily achieved via spectroscopy experiment or Rabi oscillation by scanning the Z pulse amplitude of the qubit.

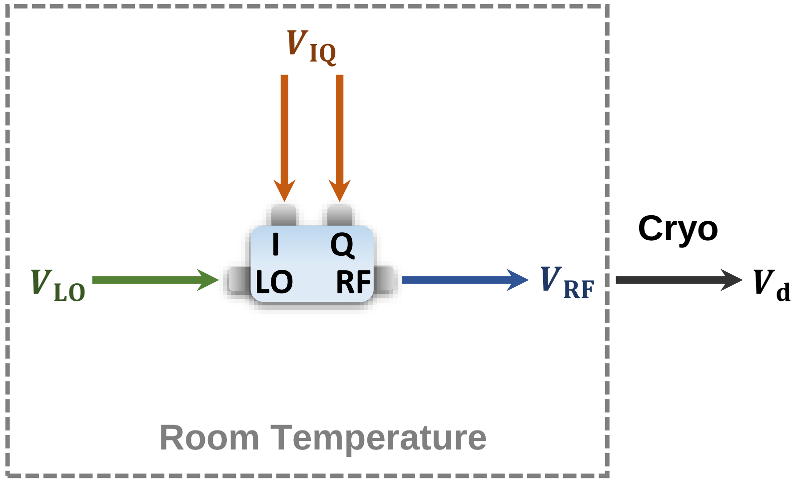

FIG. S6. **Generation of XY drive via frequency mixing.** The intrinsic local oscillation (LO) is generated from a microwave signal source, while the input IQ signals are generated from two channels of the arbitrary waveform generator. The whole circuit is mixed at room temperature and then goes into cryoelectronics (dilution refrigerator). If the amplitude of LO is fixed, the output pulse amplitude will be proportional to the amplitude of IQ signals in small amplitude cases where the IQ mixer is in a linear work region.

B. Generation and manipulation

As shown in Fig. S6, we generate XY drive pulse by using IQ mixer. The output driving pulse results from mixing the IQ signals with a intrinsic LO (Fig. S6). Although the Rabi frequency Ω is proportional to the actual driving amplitude $V_{\rm d}$, the relationship between Ω and the input amplitude of IQ signals $V_{\rm IQ}$ is not always linear due to the semiconductor nature of the IQ mixer (GaAs and similar semiconductor materials). When $V_{\rm IQ}$ is relatively small, IQ mixer is in the linear work region and $V_{\rm d} \propto V_{\rm IQ}$ satisfies. However, the strong amplitude leads to a nonlinear relationship between $V_{\rm d}$ and $V_{\rm IQ}$, so that $\Omega \propto V_{\rm IQ}$ is not valid in the saturation region. This may be caused by the velocity saturation of carriers in the IQ mixer. In order to analytically describe Ω versus $V_{\rm IQ}$, we impose the following smooth piecewise function and its inverse:

$$\Omega = \begin{cases} \eta V_{\rm IQ}, & (V_{\rm IQ} \le V_{\rm IQ}^{\rm sat}) \\ \Omega_{\rm max} - \left(\Omega_{\rm max} - \eta V_{\rm IQ}^{\rm sat}\right) e^{-\frac{\eta(V_{\rm IQ} - V_{\rm IQ}^{\rm sat})}{\Omega_{\rm max} - \eta V_{\rm IQ}^{\rm sat}}}, & (V_{\rm IQ} > V_{\rm IQ}^{\rm sat}) \end{cases} \tag{S19}$$

$$V_{\rm IQ} = \begin{cases} \frac{1}{\eta}\Omega, & (\Omega \le \eta V_{\rm IQ}^{\rm sat}) \\ V_{\rm IQ}^{\rm sat} + (\frac{\Omega_{\rm max}}{\eta} - V_{\rm IQ}^{\rm sat}) \ln\left(\frac{\Omega_{\rm max} - \eta V_{\rm IQ}^{\rm sat}}{\Omega_{\rm max} - \Omega}\right), & (\Omega > \eta V_{\rm IQ}^{\rm sat}) \end{cases} \tag{S20}$$

where η, $V_{\rm IQ}^{\rm sat}$ and $\Omega_{\rm max}$ are the parameters to be fitted. Here η is the slope in linear region that represents the Rabi frequency corresponding to the unit amplitude of XY driving (IQ signals), $V_{\rm IQ}^{\rm sat}$ denotes the critical amplitude before entering the saturation region of IQ mixer, and $\Omega_{\rm max}$ is the maximum Rabi frequency when $V_{\rm IQ} \to \infty$.

C. Origin of multi-qubit crosstalk

Now we consider two driven qubits Q_i and Q_j in the circuit (see Fig. S7). The total Lagrangian can be expressed as

$$\mathcal{L}_{\rm driven}^{(i,j)} = \sum_{q=i,j}\left(\frac{1}{2}C_q\dot{\Phi}_q^2 - \frac{\Phi_q^2}{2L_q}\right) + \frac{1}{2}C_{{\rm d},i}\left(V_{{\rm d},i}(t) - \dot{\Phi}_i\right)^2 + \frac{1}{2}C_{{\rm d},j}\left(V_{{\rm d},j}(t) - \dot{\Phi}_j\right)^2 + \frac{1}{2}C_{ij}\left(\dot{\Phi}_j - \dot{\Phi}_i\right)^2, \tag{S21}$$

where C_{ij} is the coupling capacitance. The corresponding canonical momentums are

$$\begin{bmatrix} \tilde{Q}_i \\ \tilde{Q}_j \end{bmatrix} = \begin{bmatrix} \frac{\partial \mathcal{L}_{\rm driven}^{(i,j)}}{\partial \dot{\Phi}_i} \\ \frac{\partial \mathcal{L}_{\rm driven}^{(i,j)}}{\partial \dot{\Phi}_j} \end{bmatrix} = \begin{bmatrix} C_{\Sigma_i} + C_{ij} & -C_{ij} \\ -C_{ij} & C_{\Sigma_j} + C_{ij} \end{bmatrix} \begin{bmatrix} \dot{\Phi}_i \\ \dot{\Phi}_j \end{bmatrix} - \begin{bmatrix} C_{{\rm d},i}V_{{\rm d},i} \\ C_{{\rm d},j}V_{{\rm d},j} \end{bmatrix}, \tag{S22}$$

where $C_{\Sigma_i} = C_i + C_{\mathrm{d},i}$ and $C_{\Sigma_j} = C_j + C_{\mathrm{d},j}$, and thus

$$\begin{bmatrix} \dot{\Phi}_i \\ \dot{\Phi}_j \end{bmatrix} = \frac{1}{\|\mathbf{C}\|} \begin{bmatrix} C_{\Sigma_j} + C_{ij} & C_{ij} \\ C_{ij} & C_{\Sigma_i} + C_{ij} \end{bmatrix} \begin{bmatrix} \tilde{Q}_i + C_{\mathrm{d},i} V_{\mathrm{d},i} \\ \tilde{Q}_j + C_{\mathrm{d},i} V_{\mathrm{d},i} \end{bmatrix}, \tag{S23}$$

where $\|\mathbf{C}\| = C_{\Sigma_i} C_{\Sigma_j} + C_{\Sigma_i} C_{ij} + C_{\Sigma_j} C_{ij}$ is the determinant of the capacitance matrix $\mathbf{C} = \begin{bmatrix} C_{\Sigma_i} + C_{ij} & -C_{ij} \\ -C_{ij} & C_{\Sigma_j} + C_{ij} \end{bmatrix}$. Substituting Eq. (S23) into Eq. (S21), we obtain

$$\mathcal{L}^{(i,j)}_{\text{driven}} = \frac{\tilde{Q}_i^2}{2\tilde{C}_{\Sigma_i}} + \frac{\tilde{Q}_j^2}{2\tilde{C}_{\Sigma_j}} + \frac{\tilde{Q}_i \tilde{Q}_j}{\tilde{C}_{ij}}, \tag{S24}$$

with the effective capacitance parameters

$$\tilde{C}_{\Sigma_i} = C_{\Sigma_i} + (C_{\Sigma_j} \| C_{ij}) = C_{\Sigma_i} + \frac{C_{\Sigma_j} C_{ij}}{C_{\Sigma_j} + C_{ij}}, \tag{S25}$$

$$\tilde{C}_{\Sigma_j} = C_{\Sigma_j} + (C_{\Sigma_i} \| C_{ij}) = C_{\Sigma_j} + \frac{C_{\Sigma_i} C_{ij}}{C_{\Sigma_i} + C_{ij}}, \tag{S26}$$

$$\tilde{C}_{ij} = \frac{C_{\Sigma_i} C_{ij} + C_{\Sigma_j} C_{ij} + C_{\Sigma_i} C_{\Sigma_j}}{C_{ij}}. \tag{S27}$$

Then the total Hamiltonian is given by the Legendre transformation:

$$\begin{aligned} H^{(i,j)}_{\text{driven}} &= \tilde{Q}_i \dot{\Phi}_i + \tilde{Q}_j \dot{\Phi}_j - \mathcal{L}^{(i,j)}_{\text{driven}} \\ &= \sum_{q=i,j} \left(\frac{\tilde{Q}_q^2}{2\tilde{C}_{\Sigma_q}} + \frac{\Phi_q^2}{2L_q} \right) + \frac{\tilde{Q}_i \tilde{Q}_j}{\tilde{C}_{ij}} + \left(\frac{C_{\mathrm{d},i}}{\tilde{C}_{\Sigma_i}} V_{\mathrm{d},i}(t) + \frac{C_{\mathrm{d},j}}{\tilde{C}_{ij}} V_{\mathrm{d},j}(t) \right) \tilde{Q}_i + \left(\frac{C_{\mathrm{d},j}}{\tilde{C}_{\Sigma_j}} V_{\mathrm{d},j}(t) + \frac{C_{\mathrm{d},i}}{\tilde{C}_{ij}} V_{\mathrm{d},i}(t) \right) \tilde{Q}_j. \end{aligned} \tag{S28}$$

Using canonical quantization, we introduce

$$\begin{cases} \hat{\tilde{Q}}_q = \mathrm{i} \tilde{Q}_{\text{zpf},q} (\hat{a}_q^\dagger - \hat{a}_q) \\ \hat{\Phi}_q = \Phi_{\text{zpf},q} (\hat{a}_q^\dagger + \hat{a}_q) \end{cases} \tag{S29}$$

with $q \in \{i, j\}$, $\tilde{Q}_{\text{zpf},q} = \sqrt{\hbar (\tilde{C}_{\Sigma_q} / L_{\mathrm{c},q})^{\frac{1}{2}} / 2}$ and $\Phi_{\text{zpf},q} = \sqrt{\hbar (L_{\mathrm{c},q} / \tilde{C}_{\Sigma_q})^{\frac{1}{2}} / 2}$. The quantized Hamiltonian thus is

$$\hat{H}^{(i,j)}_{\text{driven}} = \hat{H}^{(i)}_{\text{driven}} + \hat{H}^{(j)}_{\text{driven}} + \hat{H}^{(i,j)}_{\text{int}}, \tag{S30}$$

$$\hat{H}^{(q)}_{\text{driven}} = \hbar \omega_q \hat{a}_q^\dagger \hat{a}_q - \frac{E_{\mathrm{C}_q}}{2} \hat{a}_q^\dagger \hat{a}_q^\dagger \hat{a}_q \hat{a}_q + \mathrm{i} \hbar \tilde{\Omega}_q(t) (\hat{a}_q^\dagger - \hat{a}_q), \quad q \in \{i, j\}, \tag{S31}$$

$$\hat{H}^{(i,j)}_{\text{int}} = \hbar J_{i,j} (\hat{a}_i^\dagger - \hat{a}_i)(\hat{a}_j - \hat{a}_j^\dagger), \tag{S32}$$

where the parameters are

$$\hbar \omega_q = \sqrt{8 E_{\mathrm{C}_q} E_{\mathrm{J}_q}} - E_{\mathrm{C}_q}, \quad E_{\mathrm{C}_q} = \frac{\mathrm{e}^2}{2\tilde{C}_q}, \quad E_{\mathrm{J}_q} = \frac{\Phi_0^2}{4\pi^2 L_{\mathrm{c},q}}, \tag{S33}$$

$$J_{i,j} = \frac{\tilde{Q}_{\text{zpf},i} \tilde{Q}_{\text{zpf},j}}{\hbar \tilde{C}_{ij}} = \frac{\sqrt{\tilde{C}_{\Sigma_i} \tilde{C}_{\Sigma_j}}}{2\tilde{C}_{ij}} \sqrt{\left(\omega_i + \frac{E_{\mathrm{C}_i}}{\hbar} \right) \left(\omega_j + \frac{E_{\mathrm{C}_j}}{\hbar} \right)} \approx \frac{C_{ij} \sqrt{\omega_i \omega_j}}{2\sqrt{(C_{\Sigma_i} + C_{ij})(C_{\Sigma_j} + C_{ij})}}, \tag{S34}$$

$$\tilde{\Omega}_i(t) = \epsilon_{ii} \left(V_{\mathrm{d},i}(t) + \frac{\epsilon_{ij}}{\epsilon_{ii}} V_{\mathrm{d},j}(t) \right), \quad \tilde{\Omega}_j(t) = \epsilon_{jj} \left(V_{\mathrm{d},j}(t) + \frac{\epsilon_{ji}}{\epsilon_{jj}} V_{\mathrm{d},i}(t) \right), \tag{S35}$$

$$\epsilon_{ii} = \frac{\tilde{Q}_{\text{zpf},i} C_{\mathrm{d},i}}{\hbar \tilde{C}_{\Sigma_i}}, \quad \epsilon_{ij} = \frac{\tilde{Q}_{\text{zpf},i} C_{\mathrm{d},j}}{\hbar \tilde{C}_{ij}}, \quad \epsilon_{jj} = \frac{\tilde{Q}_{\text{zpf},j} C_{\mathrm{d},j}}{\hbar \tilde{C}_{\Sigma_j}}, \quad \epsilon_{ji} = \frac{\tilde{Q}_{\text{zpf},j} C_{\mathrm{d},i}}{\hbar \tilde{C}_{ij}}. \tag{S36}$$

Focusing on Eqs. (S31), (S35) and (S36), one can notice that the local driving Hamiltonian of each qubit depends on both external drive $V_{\mathrm{d},i}(t)$ and $V_{\mathrm{d},j}(t)$ due to the presence of coupling capacitance. However, this crosstalk is usually very small. As an example, we take the typical values $C_{\mathrm{d},i} = C_{\mathrm{d},j} = 30\,\mathrm{aF}$, $C_i = C_j = 85\,\mathrm{fF}$ and $C_{ij} = 0.25\,\mathrm{fF}$. Then we have $\epsilon_{ij}/\epsilon_{ii} = \epsilon_{ji}/\epsilon_{jj} \approx 0.3\%$, suggesting a low level of this crosstalk. Given the above equations, we note that the local driving Hamiltonian of each qubit is subject to both external drive $V_{\mathrm{d},i}(t)$ and $V_{\mathrm{d},j}(t)$ due to the presence of coupling capacitance.

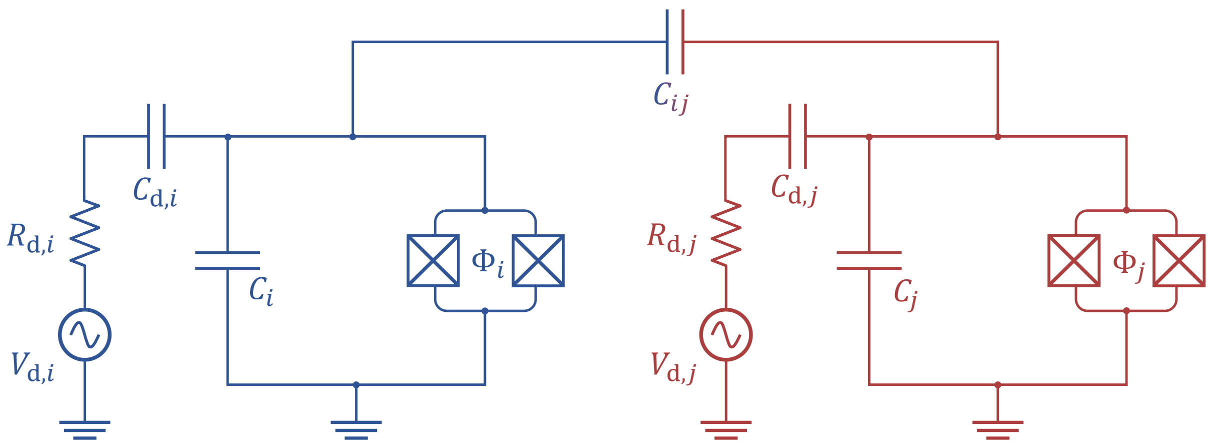

FIG. S7. **Circuit diagram of two driven transmon qubits.** Two qubits are labeled as Q_i and Q_j, which are coupled to their respective time-dependent driving voltages $V_{\mathrm{d},i}(t)$ and $V_{\mathrm{d},j}(t)$. The coupling capacitance between the two qubits is represented as C_{ij}, and Φ, C and C_{d} are the dominant mode flux, the capacitance of the qubit and the capacitance of the drive, respectively.

However, this crosstalk is usually very small. In fact, most of the crosstalk comes from the classical microwave crosstalk. The total crosstalk is the sum of the classical microwave crosstalk and the crosstalk due to the coupling capacitance. In the following, we will establish a model to describe the total crosstalk and introduce an efficient method for measuring the crosstalk matrix.

When the microwave signal travels through the medium on the chip, it can be described by the following plane wave form (the medium is assumed to be homogeneous):

$$V_{\mathrm{d}}(\mathbf{r},t) = V_{\mathrm{d}}(t)e^{\mathrm{i}\mathbf{k}\cdot\mathbf{r}}. \tag{S37}$$

Here the wave vector $\mathbf{k}$ is generally complex, namely $\mathbf{k} = \mathbf{b} + \mathrm{i}\mathbf{a}$, thus we have

$$\mathrm{i}\mathbf{k}\cdot\mathbf{r} = -\mathbf{a}\cdot\mathbf{r} + \mathrm{i}\mathbf{b}\cdot\mathbf{r}, \tag{S38}$$

where the first term is the amplitude attenuation induced by the imaginary part of $\mathbf{k}$ and the second term is the phase retardation caused by the real part. Here we define $\xi = \mathbf{a}\cdot\mathbf{r}$ is the amplitude attenuation factor and $\varphi = \mathbf{b}\cdot\mathbf{r}$ is the phase retardation.

As shown in Fig. S8, the signal $V_{\mathrm{d},i}(t)$ propagates from Q_i to Q_j with a factor $e^{-\xi_{ji}+\mathrm{i}\phi_{ji}}$ attached, which implies the classical microwave crosstalk of Q_i to Q_j. Similarly, the classical microwave crosstalk of Q_j to Q_i can be express as $V_{\mathrm{d},j}(t)e^{-\xi_{ij}+\mathrm{i}\phi_{ij}}$.

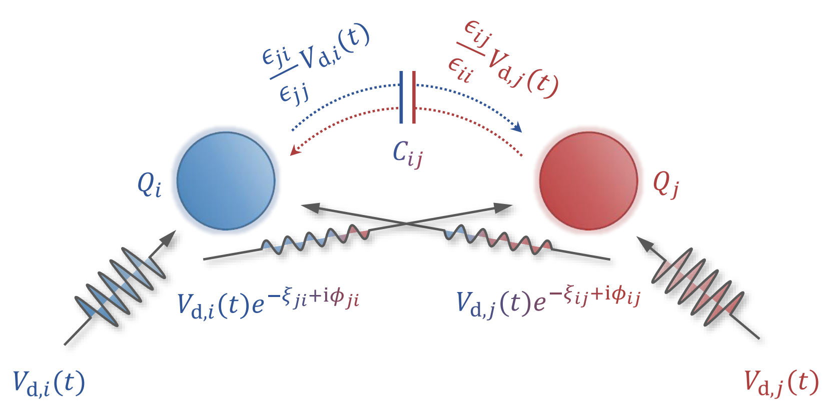

FIG. S8. **Schematic of microwave signal crosstalk.** Here, we take two qubits Q_i and Q_j as an example. Their individual driving voltages $V_{\mathrm{d},i}(t)$ and $V_{\mathrm{d},j}(t)$ induce two types of crosstalk. One type of crosstalk is due to the presence of coupling capacitance C_{ij}, which causes the crosstalk only in amplitude. The parameters ϵ_{ij} and ϵ_{ji} are explained in Eq. (S36), which depends on the coupling capacitance C_{ij} between the two qubits. The other type of crosstalk is caused by the propagation of microwave signals through the medium on the chip. According to electrodynamics, it will lead to the crosstalk both in amplitude and phase. The parameters ξ and ϕ are the amplitude attenuation factor and phase retardation of microwave propagation, respectively.

Here we also consider the crosstalk caused by the coupling capacitance as Eq. (S35). Therefore, the total signals perceived by Q_i and Q_j are

$$\tilde{V}_{\mathrm{d},i}(t) = V_{\mathrm{d},i}(t) + \frac{\epsilon_{ij}}{\epsilon_{ii}} V_{\mathrm{d},j}(t) + V_{\mathrm{d},j}(t) e^{-\xi_{ij} + \mathrm{i}\phi_{ij}}, \tag{S39}$$

$$\tilde{V}_{\mathrm{d},j}(t) = V_{\mathrm{d},j}(t) + \frac{\epsilon_{ji}}{\epsilon_{jj}} V_{\mathrm{d},i}(t) + V_{\mathrm{d},i}(t) e^{-\xi_{ji} + \mathrm{i}\phi_{ji}}, \tag{S40}$$

or written in matrix form

$$\begin{bmatrix} \tilde{V}_{\mathrm{d},i}(t) \\ \tilde{V}_{\mathrm{d},j}(t) \end{bmatrix} = \begin{bmatrix} 1 & v_{ij} e^{\mathrm{i}\varphi_{ij}} \\ v_{ji} e^{\mathrm{i}\varphi_{ji}} & 1 \end{bmatrix} \begin{bmatrix} V_{\mathrm{d},i}(t) \\ V_{\mathrm{d},j}(t) \end{bmatrix} \tag{S41}$$

with the definitions of $v_{ij} e^{\mathrm{i}\varphi_{ij}} = \epsilon_{ij}/\epsilon_{ii} + e^{-\xi_{ij}+\mathrm{i}\phi_{ij}}$ and $v_{ji} e^{\mathrm{i}\varphi_{ji}} = \epsilon_{ji}/\epsilon_{jj} + e^{-\xi_{ji}+\mathrm{i}\phi_{ji}}$. To generalize the above formula to the case of each qubit with crosstalks from all other qubits, we define the vectors $\tilde{\mathbf{V}}_{\mathbf{d}}(t) = [\tilde{V}_{\mathrm{d},1}(t), \tilde{V}_{\mathrm{d},2}(t), \ldots, \tilde{V}_{\mathrm{d},N}(t)]^T$ and $\mathbf{V}_{\mathbf{d}}(t) = [V_{\mathrm{d},1}(t), V_{\mathrm{d},2}(t), \ldots, V_{\mathrm{d},N}(t)]^T$, then

$$\tilde{\mathbf{V}}_{\mathbf{d}}(t) = \mathbf{M}_{\mathbf{V}} \mathbf{V}_{\mathbf{d}}(t), \tag{S42}$$

in which $\mathbf{M}_{\mathbf{V}}$ is the signal crosstalk matrix

$$\mathbf{M}_{\mathbf{V}} = \begin{bmatrix} 1 & v_{12} e^{\mathrm{i}\varphi_{12}} & \cdots & v_{1N} e^{\mathrm{i}\varphi_{1N}} \\ v_{21} e^{\mathrm{i}\varphi_{21}} & 1 & \cdots & v_{2N} e^{\mathrm{i}\varphi_{2N}} \\ \vdots & \vdots & \ddots & \vdots \\ v_{N1} e^{\mathrm{i}\varphi_{N1}} & v_{N2} e^{\mathrm{i}\varphi_{N2}} & \cdots & 1 \end{bmatrix}. \tag{S43}$$

D. Measurement and correction of crosstalk

To compensation the crosstalk, we need to measure the total signal crosstalk matrix and perform

$$\mathbf{V}_{\mathbf{d}}(t) = \mathbf{M}_{\mathbf{V}}^{-1} \tilde{\mathbf{V}}_{\mathbf{d}}(t), \tag{S44}$$

where $\mathbf{M}_{\mathbf{V}}^{-1}$ is the inverse matrix. However, in practice we cannot obtain $\mathbf{M}_{\mathbf{V}}$ directly, we need to characterize the crosstalk matrix of Rabi frequencies $\mathbf{M}_{\boldsymbol{\Omega}}$ and calculate $\mathbf{M}_{\mathbf{V}}$ by using

$$\mathbf{M}_{\mathbf{V}} = \boldsymbol{\epsilon} \mathbf{M}_{\boldsymbol{\Omega}} \boldsymbol{\epsilon}^{-1}, \tag{S45}$$

where $\boldsymbol{\epsilon} = \mathrm{diag}\{\epsilon_{11}, \epsilon_{22}, \ldots, \epsilon_{NN}\}$ and the crosstalk matrix of Rabi frequencies is defined as

$$\mathbf{M}_{\boldsymbol{\Omega}} = \begin{bmatrix} 1 & c_{12} e^{\mathrm{i}\varphi_{12}} & \cdots & c_{1N} e^{\mathrm{i}\varphi_{1N}} \\ c_{21} e^{\mathrm{i}\varphi_{21}} & 1 & \cdots & c_{2N} e^{\mathrm{i}\varphi_{2N}} \\ \vdots & \vdots & \ddots & \vdots \\ c_{N1} e^{\mathrm{i}\varphi_{N1}} & c_{N2} e^{\mathrm{i}\varphi_{N2}} & \cdots & 1 \end{bmatrix}. \tag{S46}$$

where c_{ij} and φ_{ij} are the amplitude and phase crosstalk coefficients to be measured.

In the linear region of IQ mixer, we actually use Eq. (S19) to describe the relationship between Rabi frequency and the input IQ signal, and thus

$$\mathbf{M}_{\mathbf{V_{IQ}}} = \boldsymbol{\eta} \mathbf{M}_{\boldsymbol{\Omega}} \boldsymbol{\eta}^{-1}, \tag{S47}$$

where $\boldsymbol{\eta}$ is given by $\boldsymbol{\eta} = \mathrm{diag}\{\eta_1, \eta_2, \ldots, \eta_N\}$ with η_i being the Rabi frequency of Q_i corresponding to the unit amplitude of IQ signals.

Now, we introduce an efficient method for characterizing c_{ij} and φ_{ij} in the crosstalk matrix $\mathbf{M}_{\boldsymbol{\Omega}}$. . Let us take an example of Q_i. As shown in Fig. S9**a**, two resonant microwave signals $\omega_{\mathrm{d},i} = \omega_{\mathrm{d},j} = \omega_{\mathrm{d}}$ are simultaneously input from the XY control lines of Q_i and Q_j. Meanwhile, Q_i is biased near the resonant frequency with the detuning $\Delta_i = \omega_i - \omega_{\mathrm{d},i}$. Due to the crosstalk, the effective Hamiltonian of Q_i under the rotation frame becomes $\hat{H}_d^{(i)} = \Delta_i \hat{\sigma}_i^+ \hat{\sigma}_i^- + \left(\tilde{\Omega}_i \hat{\sigma}_i^+ + \mathrm{H.c.}\right)/2$ with $\tilde{\Omega}_i = \Omega_i e^{-\mathrm{i}\phi_i} + c_{ij}\Omega_j e^{\mathrm{i}(\varphi_{ij} - \phi_j)}$, and the corresponding effective Rabi frequency is

$$\Omega_{\mathrm{R}}^{(i)} = \sqrt{\Delta_i^2 + \Omega_i^2 + \Omega_{ij}^2 + 2\Omega_i \Omega_{ij} \cos\left(\varphi_{ij} - \varphi_{ii}\right)}, \tag{S48}$$

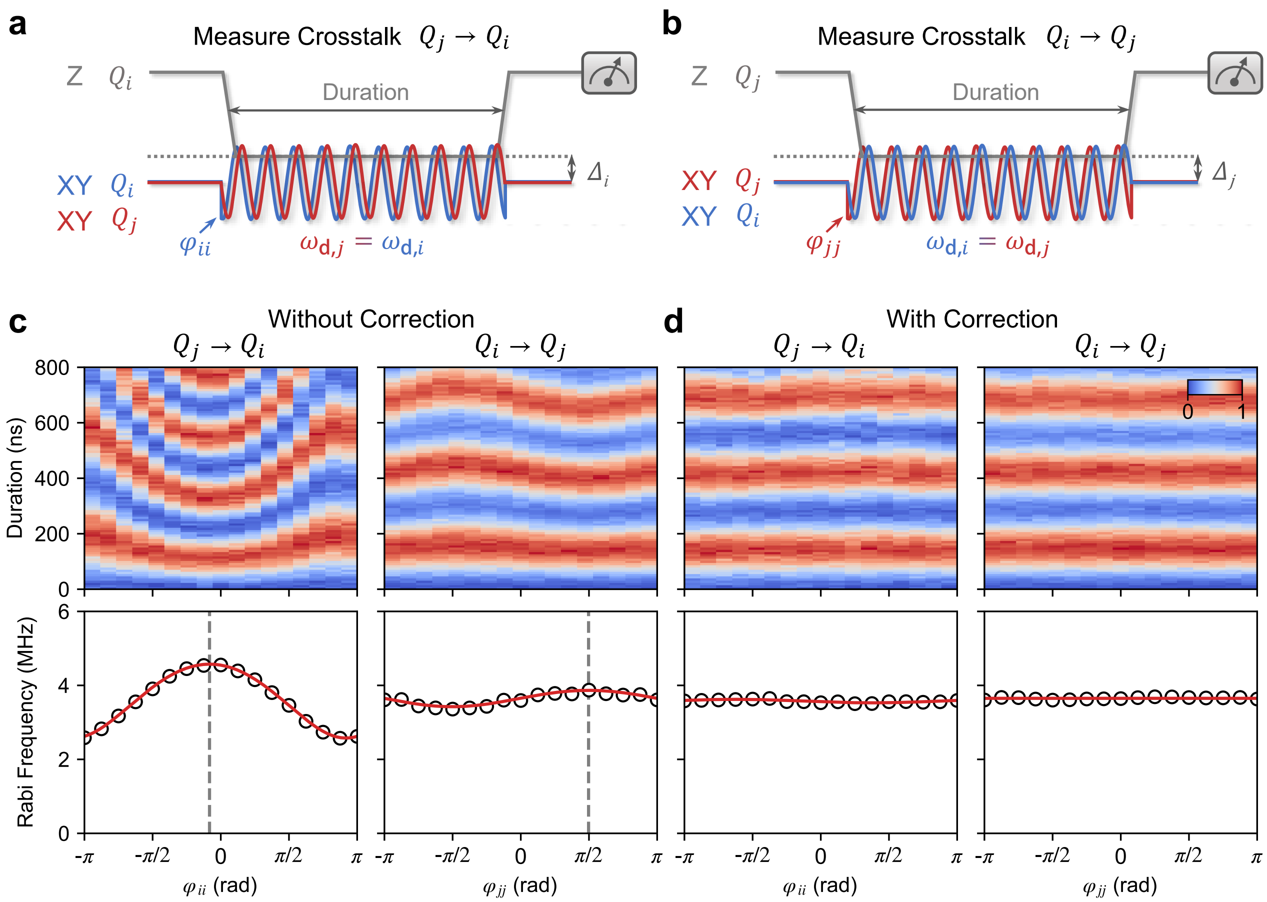

FIG. S9. **Measurement of the microwave crosstalk.** **a**, Experimental pulse sequence for measuring the crosstalk from Q_j to Q_i. **b**, Experimental pulse sequence for measuring the crosstalk from Q_i to Q_j. The parameters φ_{ii} and φ_{jj} denote the additional phases added into the XY control lines of Q_i and Q_j, respectively. The detuning between the qubit frequency and XY drive frequency is defined as $\Delta_q = \omega_q - \omega_{\mathrm{d},q}$, which is usually set to zero. **c**, Typical experimental data of measuring crosstalk without correction. **d**, Typical experimental data of measuring crosstalk with correction. The heatmap represents the probabilities of qubit in $|1\rangle$. The black hollow circle denotes the effective Rabi frequency obtained by fitting the Rabi oscillation. The red solid line is the result of fitting the effective Rabi frequency by using Eq. (S48). The grey dashed line implies the fitted crosstalk phase.

where $\Omega_{ij} = c_{ij}\Omega_j$ denotes the crosstalk Rabi frequency from Q_j to Q_i, and $\varphi_{ii} = \phi_j - \phi_i$ represents the additional XY phase added in Q_i relative to Q_j. By scanning φ_{ii} and measure the probabilities of Q_i in $|1\rangle$ as a function of the duration of XY drive, we can obtain $\Omega_{\mathrm{R}}^{(i)}$. Using Eq. (S48) to fit the results of $\Omega_R^{(i)}$, we can determine the crosstalk coefficients c_{ij} and φ_{ij}. The procedure for determining c_{ji} and φ_{ji} is similar as long as we treat Q_j as Q_i. Here we show the partial crosstalk matrix between the 24 qubits used in experiments in Fig. S10.

Supplementary Note 4. THE EFFECT OF DECOHERENCE

In this section, we discuss the effect of decoherence. Since the conservation of the particle number is essentially important for the observation of spin hydrodynamics, we pay attention to the energy relaxation effect, characterized by the coherence time T_1. To quantify the impact of decoherence on the particle number, we numerically simulate the dynamics of $n(t)$ by solving the Lindblad master equation

$$\frac{\mathrm{d}\hat{\rho}(t)}{\mathrm{d}t} = i[\hat{H}, \hat{\rho}(t)] + \sum_{j=1}^{N}(\hat{L}_j\hat{\rho}(t)\hat{L}_j^\dagger - \frac{1}{2}\{\hat{L}_j^\dagger\hat{L}_j, \hat{\rho}(t)\}), \tag{S49}$$

where $\hat{\rho}(t) = |\psi(t)\rangle\langle\psi(t)|$ is the density matrix, $\hat{H}$ is the Hamiltonian Eq. (1) in the main text, and $\hat{L}_j = \hat{\sigma}_j^-/\sqrt{T_1}$ represents the Lindblad operators for the energy relaxation, with T_1 being the energy lifetime.

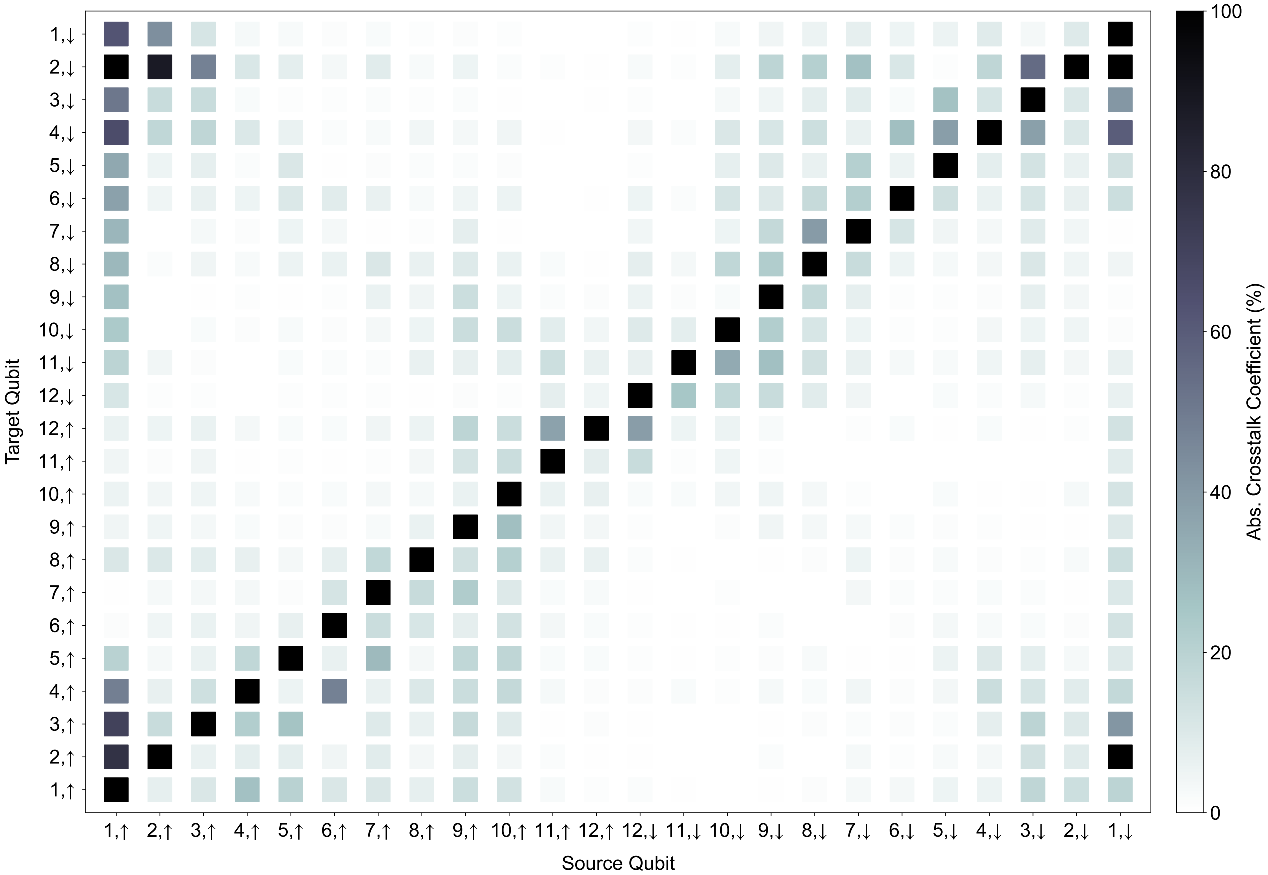

FIG. S10. **Partial crosstalk matrix of XY drive.** The heatmap represents the modulus of the crosstalk coefficient, namely $|c_{ij}|$. Here, we show the crosstalks between 24 qubits in the ladder.

For the numerical simulation, we adopt $T_1 = 32.1$ μs based on the device information shown in Table. S1. Here, we consider a ladder with the number of qubits $N = 16$, and the same initial state shown in the inset of Fig. S2**a**. We employ the stochastic Schrödinger equation to efficiently solve the Lindblad master equation (S49). First, we study the dynamics of the particle number $\langle n(t)\rangle$ under the decoherence, and the results are plotted in Fig. S11**a**. With the evolved time $t = 200$ ns, the value of $\langle n(t)/2L\rangle$ is around 0.497, suggesting that decoherence does not significantly influence the conservation of the particle number. We then numerically demonstrate that decoherence does not strongly affect the dynamics of autocorrelation function $C_{1,1}(t)$ with the evolved time up to 200 ns, and the dynamics of $C_{1,1}(t)$ simulated by solving the Lindblad master equation (S49) is more or less the same to the unitary dynamics (see Fig. S11**b**).

Supplementary Note 5. XY DRIVE APPROACH TO GENERATE HAAR-RANDOM STATES

For the Haar-random state $|\psi^R\rangle$, we can define the probability with respect to the computational basis $|k\rangle$ as $p_k = |\langle k|\psi^R\rangle|^2$. It has been shown that the distribution of the probabilities $\{p = p_k\}$ will approximate the so-called Porter-Thomas distribution [35-37]

$$\mathrm{Pr}(p) = De^{-Dp}, \tag{S50}$$

where $D = 2^N$ is the total dimension of the Hilbert space. To generate the Haar-random states via the evolution $\hat{U}_R$ in this experiment (seen in the main text or Fig. S12**a**), we bias the auxiliary qubit Q_A away from the resonance frequency and apply the XY drive pulses on all the remainder qubits Q_R participating in the resonance. The experimental pulse diagram is shown in Fig. S12**b**. After a time t_R, we perform joint readout of Q_R with N_s single-shot measurements to obtain the joint probabilities,

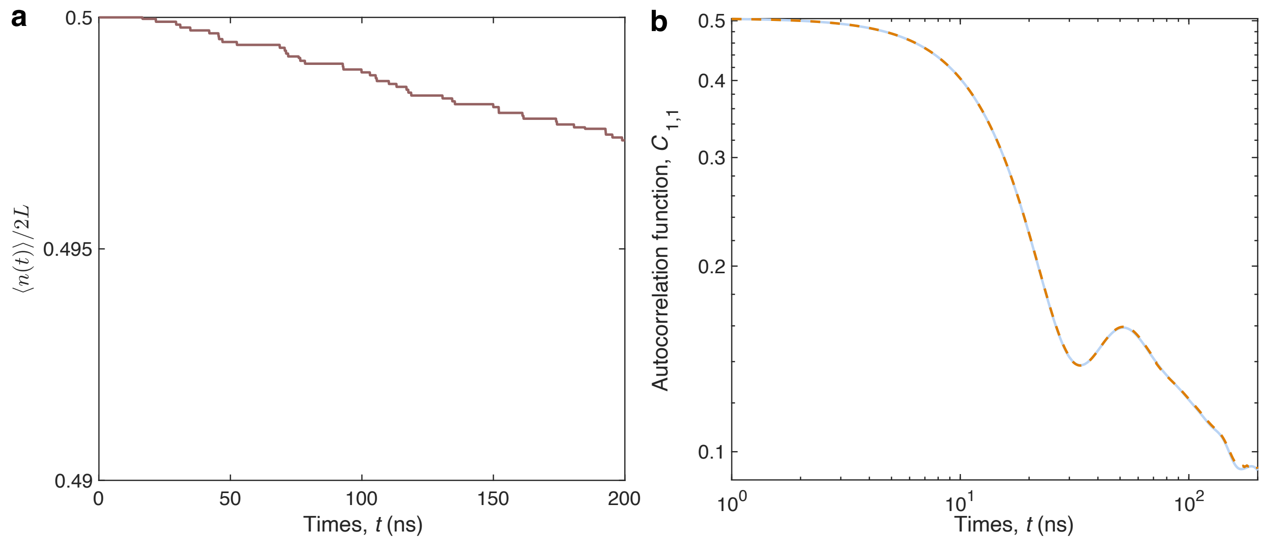

FIG. S11. **The effect of decoherence.** **a**, For the qubit ladder with a length $L = 8$ (the number of qubits $N = 16$), the dynamics of particle number $\langle n(t)\rangle$ with decoherence, i.e., energy relaxation, quantified by $T_1 = 32\ \mu$s. **b**, The dynamics of autocorrelation function $C_{1,1}(t)$ with decoherence (dashed curve), in comparison with the unitary dynamics (solid curve).

and then calculate the participation entropy

$$S_{\rm PE}(t_R) = -\sum_{k=1}^{D} p_k(t_R)\ln p_k(t_R), \tag{S51}$$

where p_n is the joint probabilities of all $D = 2^N$ bitstrings. As shown in Fig. S12**c**, the participation entropy increases rapidly and then tends to a stable value. This value matches the participation entropy of the Haar-random state, namely

$$S_{{\rm PE},|\psi^R\rangle} = -D\int_0^\infty {\rm d}p\ {\rm Pr}(p)\, p\ln p = \ln D - 1 + \gamma, \tag{S52}$$

where $\gamma \approx 0.577$ is the Euler constant. The final state after a long-time evolution is therefore closer to a Haar-random state, which shows the Poter-Thomas distribution of the bitstring joint probabilities in the statistical histogram, see Fig. S12**d**. In the experiment, we select $t_R = 200\,{\rm ns}$ to generate the Haar-random state and use this state as the initial state for subsequent interactions.

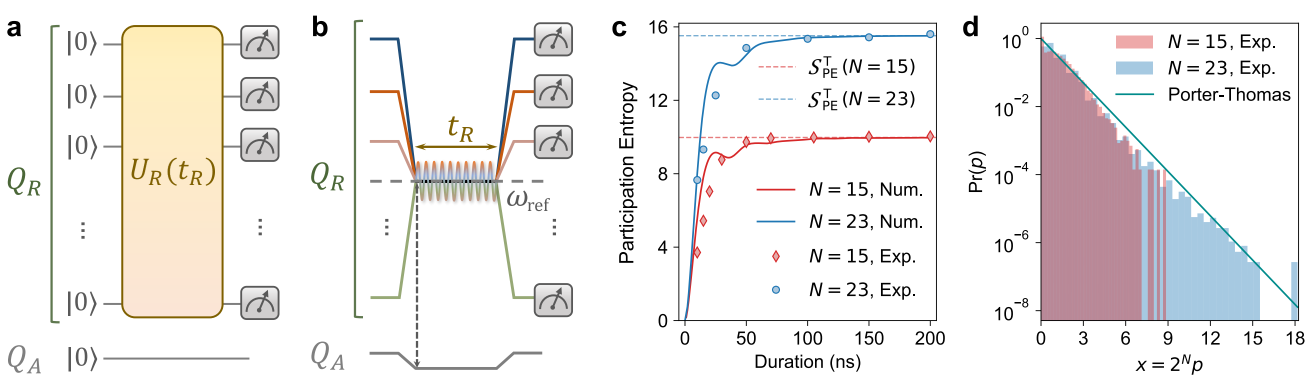

FIG. S12. **Generation and characterization of the XY drive approach to prepare the Haar-random states.** **a**, The schematic diagram of the quantum circuit. **b**, The corresponding experimental pulse sequence. We bias the auxiliary qubit Q_A away from the resonance frequency and apply the XY drive pulses on all the remainder qubits Q_R participating in the resonance at frequency $\omega_{\rm ref} \approx 4.534\,{\rm GHz}$, with a duration t_R. **c**, The evolution of participation entropy $S_{\rm PE}$ vs. the duration of XY drive. The dashed line represents the participation entropy of $N-$qubit Haar-random state. Here, we fix $Q_{1,\uparrow}$ as Q_A, and N is the total number of Q_R. **d**, The bitstring histogram of the measured $D = 2^N$ joint probabilities. The solid line shows the ideal results of Poter-Thomas distribution. For $N = 15$ and $N = 23$, we perform $N_{\rm s} = 5\times 10^5$ and $N_{\rm s} = 3\times 10^7$ single-shot measurements, respectively

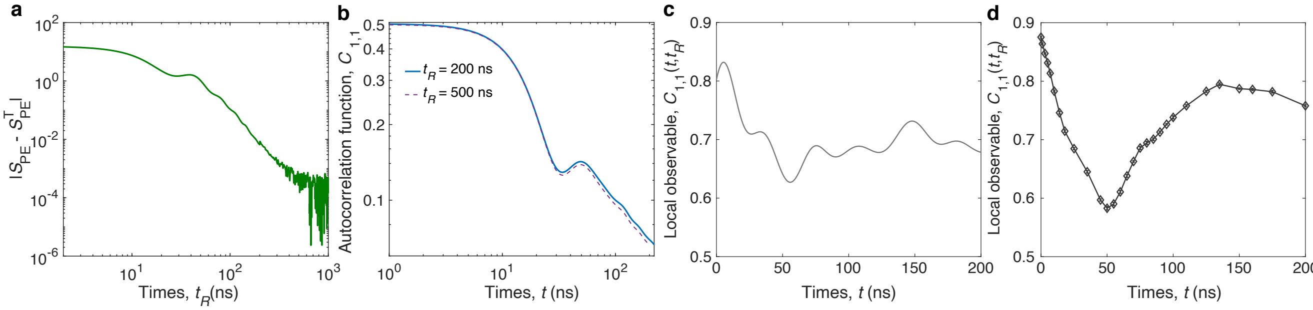

FIG. S13. **Impact of different t_R for generating Haar-random states.** **a**, The difference between the participation entropy at an evolved time t_R and that corresponding to Haar-random states S_{PE}^T, i.e., $|S_{\text{PE}}(t_R) - S_{\text{PE}}^T|$. **b**, The numerical results of autocorrelation function $C_{1,1}$ for the qubit ladder with $L = 12$, and different states generated from $\hat{U}_R(t_R)$ with $t_R = 200$ ns and 500 ns. **c**, The numerical simulation of the dynamics of the local observable $C_{1,1}(t_R, t)$ with a fixed $t_R = 15$ ns. **d**, The experimental data for the dynamics of the local observable $C_{1,1}(t_R, t)$ with a fixed $t_R = 15$ ns.

We note that the von Neumann entanglement entropy (EE) can also characterize the Haar-random states by achieving the Page value $S_{\text{Page}} \simeq \log m - m/2n$, where m and n represent the dimension of Hilbert space of the subsystem and the remainder, respectively. However, experimental measurement of EE requires additional single-qubit rotations, which can influence the accuracy of the results, especially for large system sizes. Here, we adopt the participation entropy, which can be directly measured by single-shot readout in z-direction, without rotations of qubits.

We now discuss the impact of different evolved time t_R for generating Haar-random states on the measurement of infinite-temperature autocorrelation function $C_{1,1}$. In Fig. S13**a**, we plot the numerical results of the difference between the participation entropy of the quenched state at $t = t_R$ and the participation entropy corresponding to the Haar-random state, i.e., $|S_{\text{PE}}(t_R) - S_{\text{PE}}^T|$ with the evolved time t_R up to 1 μs. It can be seen that with $t_R \simeq 200$ ns, the difference reaches $|S_{\text{PE}}(t) - S_{\text{PE}}^T| \sim 10^{-1}$, and a lower difference can be achieved for longer evolved time t. However, as shown in Fig. S13**b**, the dynamical behaviors of autocorrelation function $C_{1,1}$, with the states generated by different evolved time of $\hat{U}_R(t_R)$ with $t_R \geq 200$ ns, do not have a significant change, which indicates that the evolved time $t_R \simeq 200$ ns is sufficient to generate a faithful Haar-random state for measuring the infinite-temperature spin transport.

We then extensively study the dynamics with short t_R. In this case, the state $|\psi^R\rangle$ is far away from Haar-random states, and the local observable $\langle\psi_\beta^R|\hat{\sigma}_\alpha^z(t)|\psi_\beta^R\rangle$, with $|\psi_\beta^R\rangle = \hat{U}_R(t_R) \otimes_{i\in Q_R} |0\rangle_i$, can no longer be approximate with the infinite-temperature correlation function $\text{Tr}[\hat{\sigma}_\alpha^z(t)\hat{\sigma}_\beta^z]/D$. Consequently, we denote the quantity as local observable $C_{1,1}(t_R, t)$, with t_R and t being the evolved time for $\hat{U}_R(t_R)$ and $\hat{U}_H(t)$ shown in the quantum circuit shown in Fig. 1**c** in the main text, respectively. In Fig. S13**c** and **d**, we plot the numerical and experimental data for the dynamics of the local observable $C_{1,1}(t_R, t)$ with a fixed short time $t_R = 15$ ns, respectively. For a small $t_R = 15$ ns, after an initial drop, the local observable has an oscillation around a value larger than 0.5. This can be explained by the fact that the state $|\psi^R\rangle$ is close to the initial state $|00...0\rangle$ with small t_R, and when $t_R = 0$ and $t = 0$, actually, based on Eq. (3) of the main text, $c_{1,\uparrow;1,\uparrow} = c_{1,\uparrow;1,\downarrow} = c_{1,\downarrow;1,\downarrow} = c_{1,\downarrow;1,\uparrow} = 1$, which leads to the local observable $C_{1,1}(0, 0) = 1$.

Supplementary Note 6. FINITE-SIZE EFFECT FOR THE SPIN TRANSPORT IN THE CLEAN SUPERCONDUCTING QUBIT LADDER

In this section, we discuss the finite-size effect of the spin transport. We consider the clean superconducting qubit ladder without disorder or linear potential as an example, where the diffusive transport is expected to occur. We numerically simulate a long time evolution with the final time $t = 2000$ ns ($t\overline{J^{\parallel}} \simeq 91.2$). As shown in Fig. S14, due to the finite-size effect, the $C_{1,1}(t)$ will saturate to a stable value for long time. The time interval with the power-law decay $C_{1,1} \propto t^{-z}$ becomes longer for larger L. For $L = 8$ and 12, the estimated time intervals with the power-law decay are $t \in [50\text{ ns}, 170\text{ns}]$ and $t \in [50\text{ ns}, 450\text{ ns}]$ (highlighted by the arrows in Fig. S14), respectively. By fitting the numerical data in the time interval for $L = 8$ in $t \in [50\text{ ns}, 140\text{ ns}]$ and $L = 12$ in $t \in [50\text{ ns}, 450\text{ ns}]$, we obtain the exponent $z \simeq 0.45$ for $L = 8$ and $z \simeq 0.5$ for $L = 12$. In short, the signature of diffusive transport becomes more clear for larger system size.

Supplementary Note 7. FINITE-TIME EFFECT FOR THE SPIN TRANSPORT IN DISORDERED SYSTEMS

Here, we consider a longer evolved final time $t = 600$ ns, and study the impact of longer final time on the transport exponent

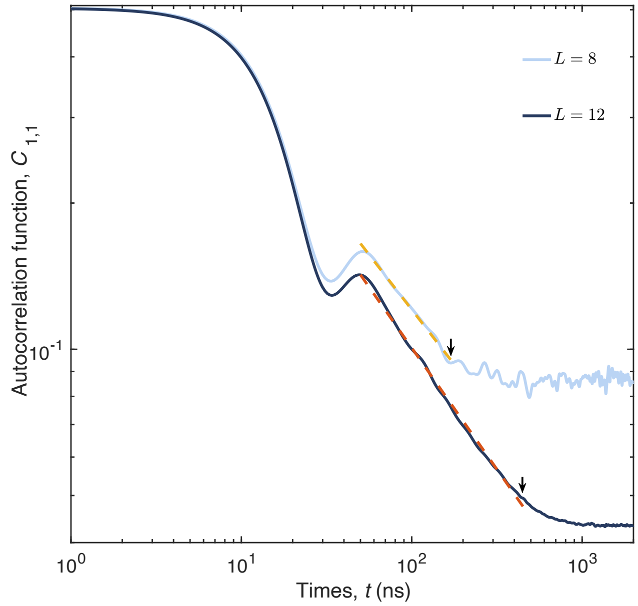

FIG. S14. **Finite-size effect.** Numerical simulation of the autocorrelation function $C_{1,1}(t)$ for the qubit ladder with different system sizes. For $L = 12$, the system consists of 24 qubits, i.e., $Q_{1,\uparrow}, ..., Q_{12,\uparrow}$ and $Q_{1,\downarrow}, ..., Q_{12,\downarrow}$. For $L = 8$, the system consists of 16 qubits, i.e., $Q_{1,\uparrow}, ..., Q_{8,\uparrow}$ and $Q_{1,\downarrow}, ..., Q_{8,\downarrow}$. The dashed lines show the power-law fitting of the numerical results in the time interval $t \in [50\text{ ns}, 170\text{ ns}]$ for $L = 8$ and $t \in [50\text{ ns}, 450\text{ ns}]$ for $L = 12$.

z obtained by the power-law fitting $C_{1,1} \propto t^{-z}$. We focus on the disordered systems with $W/2\pi = 32$ MHz and 50 MHz. With the time window $t \in [50, 200]$ ns, as shown in the Fig. 3**b** of the main text, $z \simeq 0.02$ and $z \simeq 0.13$ for $W/2\pi = 50$ MHz and 32 MHz, respectively. With the time window $t \in [50, 600]$ ns, the fittings are shown in Fig. S15**a** with $z \simeq 0.03$ and $z \simeq 0.13$ for $W/2\pi = 50$ MHz and 32 MHz, respectively. It is seen that with the time window $t \in [50, 600]$ ns, the transport exponents z are slightly larger than those for the time window $t \in [50, 200]$ ns.

We also plot the transport exponent z obtained from the power-law fitting in the time interval $t \in [t_i, t_f]$, with a fixed initial time $t_i = 20$ ns, and different t_f in Fig. S15**b** and **c** for $W/2\pi = 32$ MHz and 50 MHz, respectively. It is shown that with longer final time t_f, the transport exponent z exhibits a propensity to increase.

Supplementary Note 8. ADDITIONAL NUMERICS AND DISCUSSIONS

In this section, we numerically study another type of autocorrelation functions which are defined by the average over a product state $|\psi_0\rangle$. In the main text, we focus on the infinite-temperature autocorrelation function $C_{\mathbf{r},\mathbf{r}} = \text{Tr}[\hat{\rho}_{\mathbf{r}}(t)\hat{\rho}_{\mathbf{r}}]/D$ with D being the dimension of the Hilbert space. Alternatively, one can also consider the autocorrelation function average over a product state $|\psi_0\rangle$, i.e.,

$$C_{\mathbf{r},\mathbf{r}}(|\psi_0\rangle) = \langle\psi_0|\hat{\rho}_{\mathbf{r}}(t)\hat{\rho}_{\mathbf{r}}|\psi_0\rangle. \tag{S53}$$

Here, we reveal that the autocorrelation function $C_{\mathbf{r},\mathbf{r}}(|\psi_0\rangle)$ cannot show generic properties of spin transport, and the dynamics of $C_{\mathbf{r},\mathbf{r}}(|\psi_0\rangle)$ is highly dependent on the choice of $|\psi_0\rangle$.

We consider the titled superconducting qubit ladder consisting of 24 qubits with $W_S/2\pi = 60$ MHz, and the slope of the linear potential $\gamma/2\pi \simeq 11$ MHz. Three chosen product states $|\psi_0\rangle$ for the autocorrelation function (S53) are shown in Fig. S16**a**. The product states with the domain wall number $n_{\text{dw}} = 10$, 4, and 2 are labeled as $|\psi_0^{(10)}\rangle$, $|\psi_0^{(4)}\rangle$, and $|\psi_0^{(2)}\rangle$, respectively. It can be directly calculated that the $\langle\psi_0^{(10)}|\hat{H}|\psi_0^{(10)}\rangle = \langle\psi_0^{(4)}|\hat{H}|\psi_0^{(4)}\rangle = \langle\psi_0^{(2)}|\hat{H}|\psi_0^{(2)}\rangle$. The results of the time evolution of $C_{\mathbf{r},\mathbf{r}}(|\psi_0\rangle)$ with $\mathbf{r} = 1$ are presented in Fig. S16**b**. It is seen that for the product state with $n_{\text{dw}} = 2$, the decay of $C_{\mathbf{r},\mathbf{r}}(|\psi_0\rangle)$ can be neglected, while the decay becomes stronger when we consider $C_{\mathbf{r},\mathbf{r}}(|\psi_0\rangle)$ with $n_{\text{dw}} = 4$ and 10.

Actually, in ref. [15], it has been shown that the infinite-temperature autocorrelation function can be expanded as

$$C_{\mathbf{r},\mathbf{r}} = \frac{1}{D}\text{Tr}[\hat{\rho}_{\mathbf{r}}(t)\hat{\rho}_{\mathbf{r}}] = \frac{1}{D}\sum_{k=1}^{D}\langle k|\hat{\rho}_{\mathbf{r}}(t)\hat{\rho}_{\mathbf{r}}|k\rangle, \tag{S54}$$

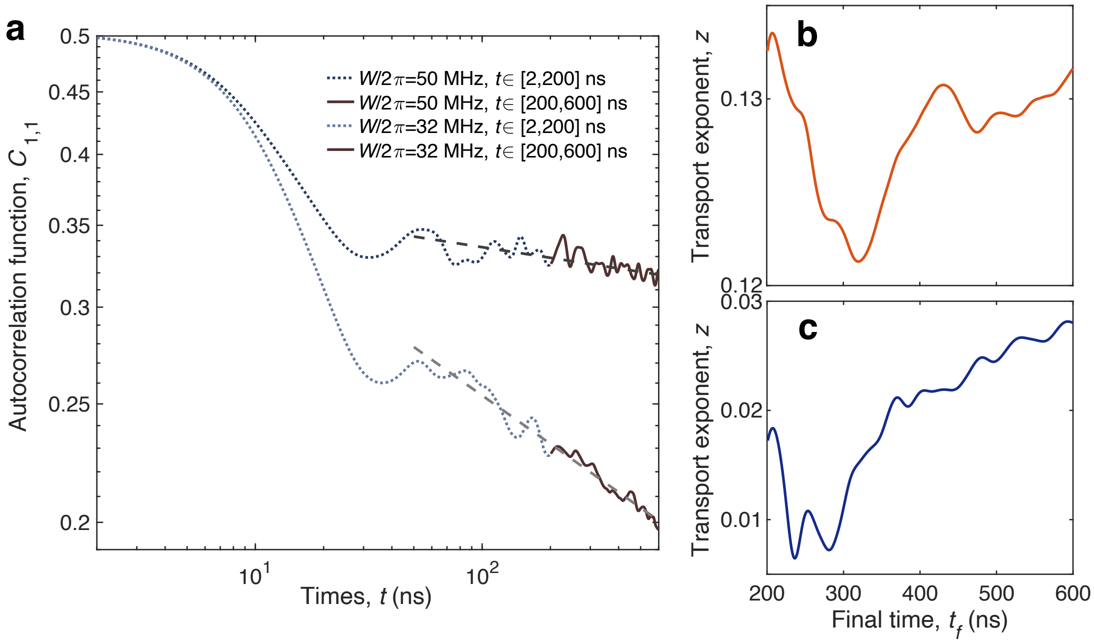

FIG. S15. **Impact of the finite-time effect.** **a**, Numerical results for the time evolution of autocorrelation function $C_{1,1}(t)$ for the qubit ladder with $L=12$, and two values of disorder strengths $W/2\pi = 32$ MHz and 50 MHz. The evolved time is up to a longer time $t = 600$ ns. The dashed lines show the power-law fitting $C_{1,1} \propto t^{-z}$. **b**, For the disordered system with $W/2\pi = 32$ MHz, the transport exponent z obtained from the power-law fitting for the numerical results with the time interval $t \in [t_i, t_f]$, $t_i = 50$ ns, and different t_f. **c** is similar to **b**, but for the disordered system with $W/2\pi = 50$ MHz.

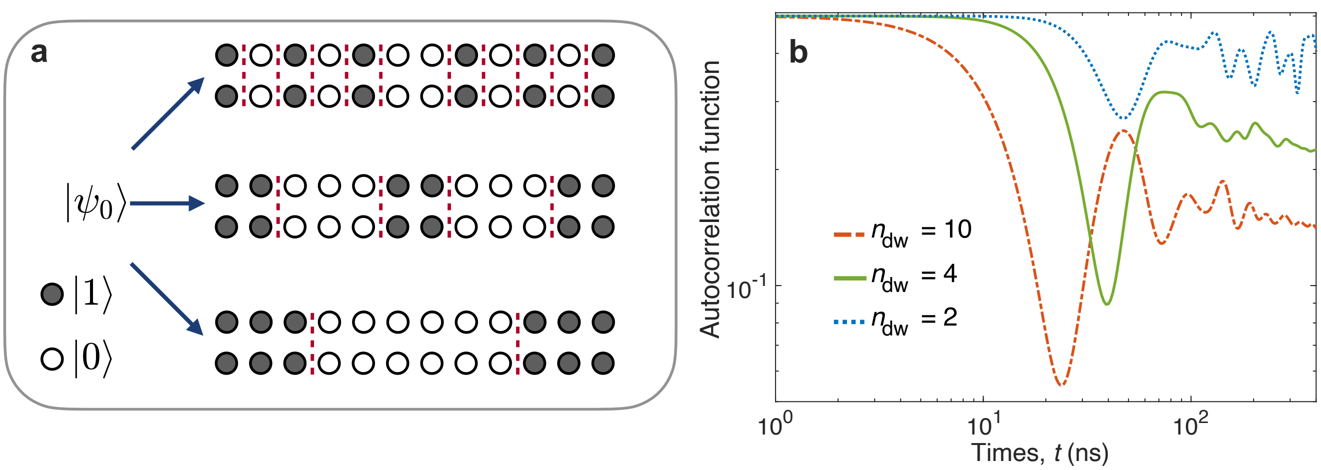

FIG. S16. **Additional numerical results for the spin transport on the titled superconducting qubit ladder.** **a**, Schematic diagram of three different product states $|\psi_0\rangle$ for the definition of the autocorrelation function $C_{1,1} = \langle\psi_0|\hat{\rho}_1(t)\hat{\rho}_1|\psi_0\rangle$. From the top to bottom, the domain wall number of product states $|\psi_0\rangle$ is $n_{\rm dw} = 10$, 4, and 2, respectively. **b**, Time evolution of the autocorrelation function $C_{1,1} = \langle\psi_0|\hat{\rho}_1(t)\hat{\rho}_1|\psi_0\rangle$ with the product states shown in **a** for the titled superconducting qubit ladder with $W_S/2\pi = 60$ MHz.

where $|k\rangle = |\sigma_{1,\uparrow}\sigma_{2,\uparrow}...\sigma_{12,\uparrow};\sigma_{1,\downarrow}\sigma_{2,\downarrow}...\sigma_{12,\downarrow}\rangle$ is the product states in the σ^z basis. As shown in Fig. S16**b**, a single term $\langle k|\hat{\rho}_{\mathbf{r}}(t)\hat{\rho}_{\mathbf{r}}|k\rangle$ in (S54) cannot capture the properties of infinite-temperature spin transport. In our work, we employ the quantum circuit shown in Fig. 1**c** to directly measure the infinite-temperature autocorrelation function, without the need of sampling different product states.